Journal of Alloys and Compounds 839 (2020) 155614

Contents lists available at ScienceDirect

Journal of Alloys and Compounds

journal homepage: http://www.elsevier.com/locate/jalcom

# Graphene induced growth of $Sb_2WO_6$ nanosheets for high-performance pseudocapacitive lithium-ion storage

Fei Wang [a], Yong Liu [a, **], Huijie Wei [a], Guangxin Wang [a], Fengzhang Ren [a, ***], Xianming Liu [b], Min Chen [c], Alex A. Volinsky [d], Shizhong Wei [a], Yan-Bing He [e, *]

[a] *Provincial and Ministerial Co-construction of Collaborative Innovation Center for Non-ferrous Metal new Materials and Advanced Processing Technology, National Joint Engineering Research Center for Abrasion Control and Molding of Metal Materials, Henan Key Laboratory of Non-Ferrous Materials Science & Processing Technology, School of Materials Science and Engineering, Henan University of Science and Technology, Luoyang, 471023, PR China*
[b] *Key Laboratory of Function-oriented Porous Materials, College of Chemistry and Chemical Engineering, Luoyang Normal University, Luoyang, 471934, PR China*
[c] *School of Materials Science and Energy Engineering, Foshan University, Foshan, 528000, PR China*
[d] *Department of Mechanical Engineering, University of South Florida, Tampa, FL, 33620, USA*
[e] *Shenzhen Geim Graphene Center, Tsinghua Shenzhen International Graduate School, Tsinghua University, Shenzhen, 518055, PR China*

## ARTICLE INFO

*Article history:*
Received 12 February 2020
Received in revised form
6 May 2020
Accepted 12 May 2020
Available online 20 May 2020

*Keywords:*
$Sb_2WO_6$ nanosheets
Graphene induced growth
Hybrid clusters
Pseudocapacitive
Anode
Lithium-ion batteries

## ABSTRACT

Transition metal oxides with the Aurivillius structure have been studied as electrode materials in lithium-ion batteries (LIBs) owing to their high capacity and proper redox voltage. With the opened Aurivillius structure, the antimony tungstate ($Sb_2WO_6$, SWO) constituted of $\{Sb_2O_2\}^{2n+}$ and $\{WO_4\}^{2n-}$ is rarely used as negative electrode material for lithium-ion batteries. Herein, the SWO nanosheets/reduced graphene oxide (rGO) hybrid clusters were synthesized, and their electrochemical performances, kinetics and lithium storage mechanism were systematically studied as negative electrode materials for LIBs. Results show that the graphene oxide (GO) not only restricts the growth of layered-structure SWO, but also induces SWO growth along (002) lattice plane and changes SWO particles to SWO nanosheets. The strong interaction between SWO nanosheets and rGO greatly improve conductivity and structure stability of SWO nanosheets/rGO hybrid clusters, which also can efficiently alleviate agglomeration and volume change of SWO nanosheets during cycling. Meanwhile, the dominating pseudocapacitive contribution (78.2% at 0.8 mV $s^{-1}$) effectively enhanced the electrochemical performance. As an anode material for LIBs, the SWO nanosheets/rGO hybrids deliver a high specific capacity of 1141 mAh $g^{-1}$ at a current density of 0.2 A $g^{-1}$, and their specific discharge capacity is 595 mAh $g^{-1}$ after 130 cycles at 0.2 A $g^{-1}$. This work demonstrates that the SWO nanosheets/rGO hybrid clusters are a promising negative electrode material for high-energy-density LIBs.

## 1. Introduction

Lithium-ion batteries (LIBs) are generally applied in the fields of portable devices, electric cars and smart grids because of high working voltage and long cycle life [1–7]. Although batteries energy density grew very drastically in recent years, it still unable to meet people's ever-growing demands [5,8–10]. As the most popular negative material for LIBs, graphite has an unsatisfactory theoretical specific capacity (~372 mAh $g^{-1}$). The relative low capacity limits its further developments for high energy density LIBs [11–15][15]. As alternatives of graphite, metal oxides have been intensively studied as anode materials for LIBs because of simple preparation method, economical raw materials, and excellent lithium storage capacity [16–19]. For example, the core-shell nanocomposites of porous $TiO_2$ nanobelts @$Sn_3O_4$ nanosheets fabricated by two-step hydrothermal reactions exhibited improved cycling performance [17]. Moreover, multivalent metal oxides with a high electrochemical activity resulting in complex compositions could deliver two to three times higher specific capacity than the graphite [18,19]. Nevertheless, there are still inherent drawbacks

---

* Corresponding author.
** Corresponding author.
*** Corresponding author.

*E-mail addresses:* liuyong209@haust.edu.cn (Y. Liu), renfz@haust.edu.cn (F. Ren), he.yanbing@sz.tsinghua.edu.cn (Y.-B. He).

https://doi.org/10.1016/j.jallcom.2020.155614

for metal oxides of inferior conductivity and large volume changes [20]. Many efforts have been undertaken to address these problems [21–23]. For instance, Lee et al. reported $WO_x$/carbon nanofibers synthesized by electrospun reduction to improve the electrode material conductivity and mechanical stability, exhibiting stable cycling and rate performance [21]. Sun and co-workers synthesized $CoFe_2O_4$@CMK-5 composites via nanocasting method, and applied it as anode for LIBs, which exhibited 836 mAh $g^{-1}$ after 100 cycles [22].

As a kind of mixed transition metal oxides, antimony tungstate ($Sb_2WO_6$, SWO) has been widely investigated in gas sensors, catalysis, and other fields, on account of its unique layered structure and physicochemical properties [24–26]. Whereas, SWO has rarely been systematically investigated as negative material for LIBs [27,28]. For example, Cruz et al. investigated the lithium insertion in $Sb_2WO_6$ with Aurivillius framework [27], and in our previous work, the $Sb_2WO_6$ nanosheets have been synthesized and studied as anode materials for LIBs. However, their electrochemical performances were not satisfactory due to their inferior electronic conductivity [28]. In addition, SWO synthesized by simple antimony source and tungsten source displays nanoparticles or micro-nanoparticles in most cases [25,29], which presents severe particle aggregation behaviour. Hence, it is urgent to develop architectural design to effectively relieve SWO nanoparticles aggregation and improve SWO electronic conductivity for an anode material for high-performance LIBs [30].

Herein, SWO nanosheets/reduced graphene oxide (SWO/rGO) hybrid clusters were synthesized by simple solvothermal method and their electrochemical performances, kinetics and lithium storage mechanism for LIBs were systematically investigated. The SWO/rGO clusters structure could efficiently prevent SWO particles agglomeration. Interestingly, it is found that rGO can regulate morphology of SWO which transforms from particles to nanosheets. The interactional oxygenated groups on rGO surface and positive metal ions of SWO precursor restricted growth of SWO and induced SWO growth along its (002) lattice plane to form nanosheets. The nanosheets clusters structure could effectively improve the electronic conductivity for high rate performance. In addition, the strong interaction between rGO and SWO can construct a long-range conductive network. When investigated as negative electrode materials for lithium-ion batteries, optimised SWO/rGO hybrid clusters exhibits a high specific capacity of ~1141 mAh $g^{-1}$ at the current density of 0.2 A $g^{-1}$, and their specific discharge capacity is 577.1 mAh $g^{-1}$ after 150 cycles at 0.2 A $g^{-1}$.

## 2. Experimental

### 2.1. Synthesis of SWO/rGO clusters

GO was prepared from graphite powder according to the modified Hummers' method. The SWO/rGO clusters were synthesized through one-step solvothermal method. Typically, 0.231 g $SbCl_3$ and 0.166 g $Na_2WO_4{\bullet}2H_2O$ were dispersed in 10 mL ethylene glycol (EG), respectively, under vigorous stirring and keeping for 30 min. In addition, 30 mg GO was uniformly dispersed in 10 mL distilled water by ultrasonic agitation for 1 h. Then, the above three solutions were transferred into 50 mL Teflon-lined autoclave and stirred for another 30 min, and heated at 160 °C for 10 h. As a contrast, SWO with different GO additive amounts (0 mg, 20 mg, 40 mg, marked as SWO, SWO/rGO-20, SWO/rGO-40, respectively) were synthesized by the same route.

### 2.2. Materials characterization

The phase composition and crystal structure of prepared samples were characterized by X-ray diffraction (XRD, Bruker D8 ADVANCE, Cu Kα source). The morphology, energy disperse X-ray spectroscopy (EDX) and element mapping of prepared materials were investigated by scanning electron microscopy (SEM, JSM-5601LV, JEOL, Akishima, Japan). The microstructure was characterized by transmission electron microscopy (TEM, JSM-2100F, 200 kV, Hitachinaka, Naka, Japan). The rGO contents in SWO/rGO materials were analyzed by TGA (Mettler DSC3) in air with the temperature ranging from room temperature to 800 °C at the heating rate of 5 °C $min^{-1}$. Raman spectra were conducted on HORIBA Jobin Yvon LabRAM HR800 using a 532 nm laser as the excitation source to investigate the order degree of carbon in SWO/rGO-30. The surface area was measured by the Brunauer-Emmett-Teller (BET) method on a micromeritics ASAP2020 nitrogen adsorption-desorption instrument. The X-ray photoelectron spectroscopy (XPS) analysis was taken using an ESCALAB 250Xi (Thermo Fisher) spectrometer employing an Al Kα X-ray source to measure chemical states of elements in products. To investigate the reaction mechanism during insertion/extraction of Lithium-ion in SWO, ex-situ XRD experiments were conducted.

### 2.3. Electrochemical performance

To examine electrochemical performance of as-prepared samples, SWO/rGO and SWO electrodes were assembled into coin cells (type CR2025). Specifically, the active materials (70 wt%), super P (20 wt%) and the binder polyvinylidene fluoride (PVDF, 10 wt%) were mixed into N-methyl pyrrolidone (NMP) to form a homogeneous slurry by stirring for 8 h. After that, the steady slurry was coated onto conductive copper foil and dried at 80 °C overnight in vacuum oven. The samples were cut into wafers with 12 mm diameter, and the loading mass was about 1 mg $cm^{-2}$. The coin cells with lithium foil as a counter electrode were assembled in a glove box with low water and oxygen content (lower than 1 ppm). During the assembly, 1 M $LiPF_6$ in ethylene carbonate (EC) and dimethyl carbonate (DMC) (1:1 in volume) was used as the electrolyte, and Celgard 2400 was used as separator. The galvanostatic charge-discharge performance was characterized by the LAND system (CT2001A) at various current densities. Cyclic voltammetry tests were taken by using an electrochemical workstation (CHI660C, Chenhua Instrument, Shanghai) ranging 0.01–3.0 V at 0.2–2 mV $s^{-1}$. Electrochemical impedance spectra (EIS) measurements were performed on CHI660C ranging 0.01 Hz to 100 000 Hz.

## 3. Results and discussion

SWO/rGO composites were synthesized through solvothermal method. As outlined in Scheme 1, the stable $Sb^{3+}$-EG and $WO_4^{2-}$-EG complexes were formed after $SbCl_3$ and $Na_2WO_4{\cdot}2H_2O$ were uniformly dispersed in EG by reason of the strong coordination between metal ions and EG Ref. [26]. GO was added into mixture before the solvothermal process. As a result, the SWO/rGO clusters were formed by planar-confined growth of oxygenated groups on GO surface and positive metal ions of SWO precursor. To investigate the formation process of SWO/rGO, SWO/rGO-30 with solvothermal time of 0.5 h, 1 h, 2 h, and 6 h were prepared. The corresponding SEM images and XRD pattern are shown in Fig. S1. With the increasing solvothermal time, the morphology of SWO/rGO-30 changed from powdery precursor (Fig. S1a) to spherical particles (Figs. S1b and c), further to layered structure (Figs. S1d and e). With the solvothermal time increasing to 2 h, the product crystalline peaks appeared in XRD pattern (Fig. S1f) and the partial $Sb_2WO_6$/rGO changed from amorphous particles to crystalline nanosheets. Finally, after solvothermal reaction for 10 h, the products completely transformed to nanosheets (Fig. 2c).

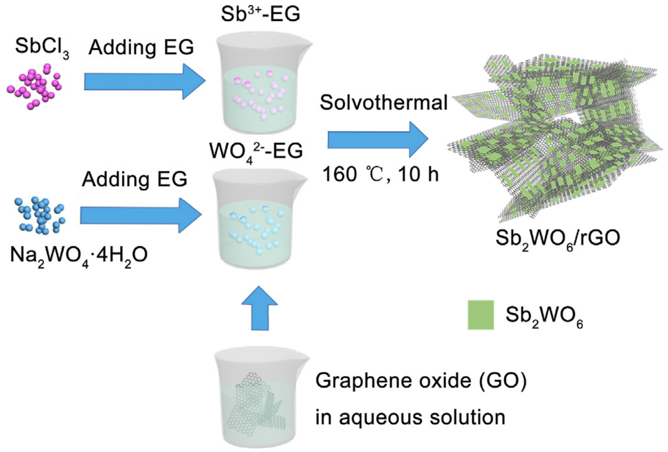

**Scheme 1.** Schematic illustration of $Sb_2WO_6$ (SWO)/rGO clusters preparation process.

Fig. 1a shows that XRD patterns of as-synthesized $Sb_2WO_6$ and $Sb_2WO_6$/rGO samples prepared with various GO addition amounts match well with the standard XRD pattern of $Sb_2WO_6$ (JCPDS No. 50-1553) and no impurity could be detected. Moreover, with the increase of GO addition amount, the intensity of (211) peak increases, which may be ascribed to the effect of rGO-induced growth [30,31]. The SWO grows along its (002) lattice plane in SWO/rGO hybrids, which is verified according to XRD pattern in Fig. 1b. The intensity ratios of (002) to (211) peak in SWO, SWO/rGO-20, SWO/rGO-30, SWO/rGO-40 are 1.12, 1.40, 1.46, 1.55, respectively (Fig. S2). Obviously, the intensity of (002) peak increases with the increase of GO addition amount. In addition, compared to the SWO, the (211) peak in the XRD pattern of the SWO/rGO-30 shifts from 27.28° to 25.81° (Fig. 1b), corresponding to the (211) interplanar spacing increasing from 0.3271 nm to 0.3453 nm. The expanded interplanar spacing may be beneficial for ion transportation in SWO/rGO-30 anode. As shown in Fig. 1c, there are three plateaus at 200 °C, 400 °C, and 600 °C in the TGA curve, The weight-loss before 200 °C is attributed to the remove of water [32]. And the weight-loss in the range of 200 °C–400 °C may be attributed to the remove of functional groups of hydroxyl, carbonyl and epoxy groups on rGO surface [33]. And the weight-loss ranging 400 °C–600 °C should be ascribed to the oxidation of rGO [34]. Based on above analysis, the rGO was removed in the range of 200 °C–600 °C, and its weight is calculated to be ~6.86 wt% in SWO/rGO-30 sample after anhydration. Similarly, the proportions of rGO in SWO/rGO-20 and SWO/rGO-40 were measured to be 5.66% and 8.19% (Fig. S3), respectively. In the Raman spectra of pristine SWO and SWO/rGO-30 (Fig. 1d), the spectra peaks centered at 719, 882, and 1566 cm$^{-1}$ can be assigned to SWO phase. These peaks of the

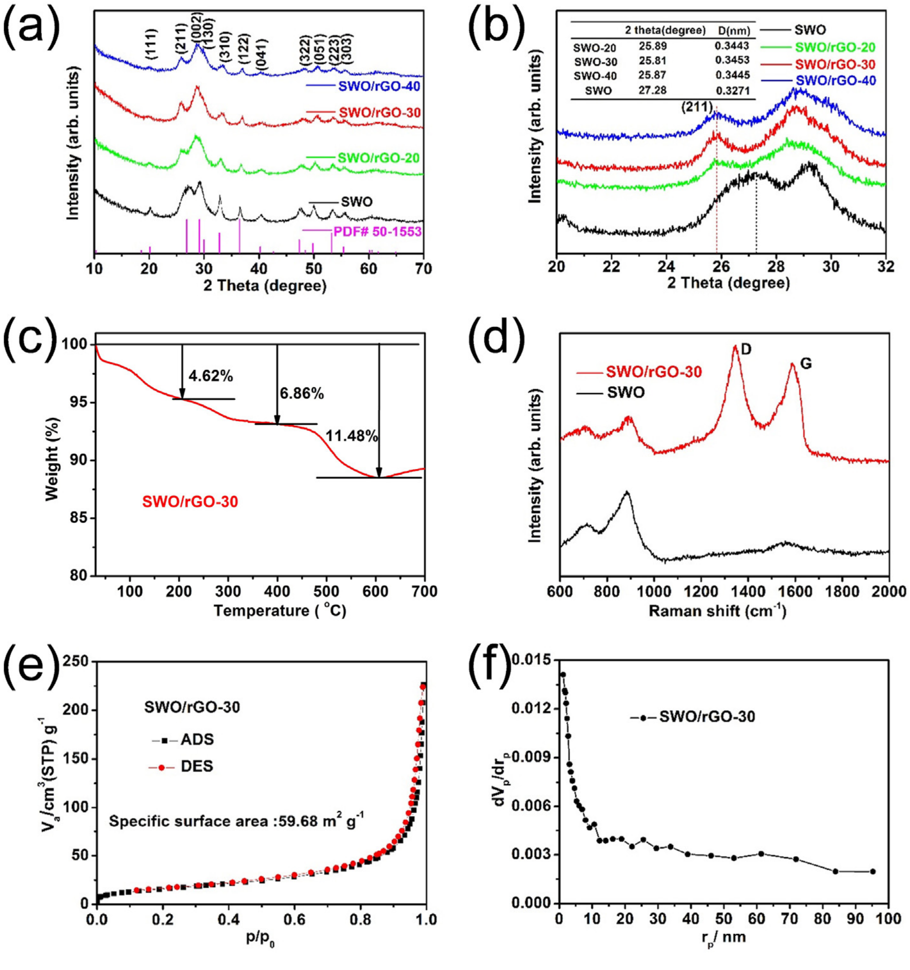

**Fig. 1.** (a) X-ray diffraction patterns (XRD) of SWO with different rGO content, (b) XRD patterns of prepared SWO/rGO composites for the 2 theta angle ranging from 20° to 32°,(c) Thermogravimetry (TG) curve of the prepared SWO/rGO-30, (d) Raman spectra of pristine SWO and SWO/rGO-30, (e) Nitrogen adsorption/desorption isotherms of SWO/rGO-30 and (f) pore size distribution of SWO/rGO-30.

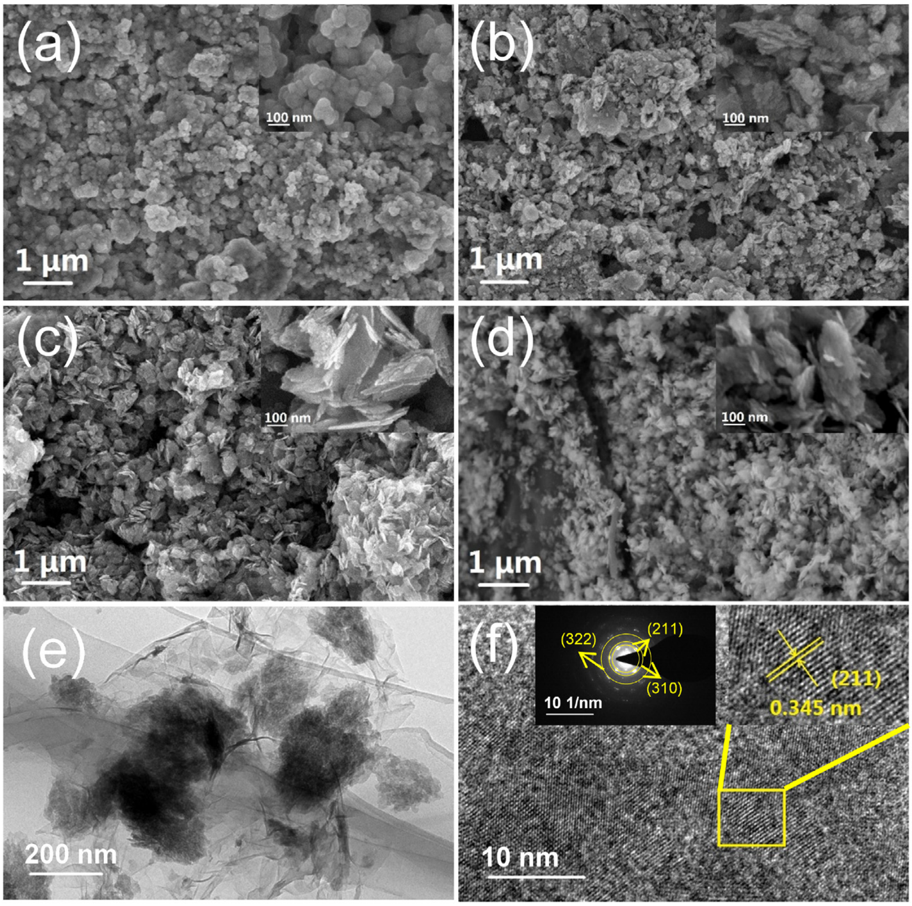

**Fig. 2.** Scanning electron microscopy images of (a) SWO, (b) SWO/rGO-20, (c) SWO/rGO-30, (d) SWO/rGO-40, (e) Transmission electron microscopy image and (f) High-resolution transmission electron microscopy images of SWO/rGO-30 (two insets are selected area electron diffraction pattern (left) and partial enlarged detail of High-resolution transmission electron microscopy image (right)).

SWO/rGO-30 have a slight shift, which could be attributed to the interaction of SWO and rGO. Two peaks at ~1343 and ~1587 $cm^{-1}$ are D band and G band in SWO/rGO-30, respectively [35]. The $I_D/I_G$ ratio of SWO/rGO-30 is about 1.14, indicating the lattice disorder of rGO [35]. And the defective rGO in SWO/rGO-30 may be beneficial for improving the electrochemical properties of SWO/rGO-30. Nitrogen adsorption/desorption isotherms and Barrett-Joyner-Halenda pore size distribution curves of as-synthesized SWO/rGO-30 present that a hysteresis loop in the relative-pressure range of 0.4–1, which is in accordance with the type IV isotherm that is typical for mesoporous materials (Fig. 1e and f). The specific surface area of SWO/rGO-30 is ~59.68 $m^2$ $g^{-1}$. This mesoporous structure is favorable for transportation and storage of lithium-ions [36]. Accordingly, the BET surface and Barrett-Joyner-Halenda (BJH) pore distribution of the pristine SWO was tested, as shown in Fig. S4. The high BET surface of 56.66 $m^2$ $g^{-1}$ in Fig. S3a and dominant mesoporous distribution in Fig. S3b are attributed to nanoscale SWO particles.

SEM images of SWO and SWO/rGO samples with various GO addition amounts are depicted in Fig. 2a–d. The pristine SWO shows submicron particles that composed of smaller particles (Fig. 2a). The SWO/rGO-20 microstructure (Fig. 2b) mainly consists of stacked layer and agglomerated block, indicating that the SWO/rGO with 20 mg GO content could transform SWO particle to SWO sheet to a certain extent. Whereas, the morphology of SWO/rGO-20 is uneven which may be due to low GO content in SWO. Interestingly, SWO/rGO-30 with addition of 30 mg GO has nanosheet-cluster structure with submicron length and about 10 nm thickness (Fig. 2c). Compared with the morphology of SWO/rGO-20, the formation of SWO nanosheets/rGO-30 clusters may be ascribed to the induced effects of GO during growth of SWO. To ensure the optimal GO content, SWO/rGO-40 with 40 mg GO was also synthesized. The morphology of SWO/rGO-40 shows both layered sheets and blocks (Fig. 2d), indicating that the excessive GO content might not effectively induce the SWO growth [37,38]. The TEM image of SWO/rGO-30 shows that layered SWO is uniformly distributed in rGO (Fig. 2e). This architecture could effectively prevent aggregation of SWO nanosheets as well as ensure excellent conductivity of SWO/rGO composite. The HRTEM image shows that the measured interplanar spacing is 0.345 nm (right inset in Fig. 2f), which is in agreement with the (211) plane in the standard card PDF# 50-1553. The selected area electron diffraction (SAED) pattern of SWO/rGO-30 in Fig. 2f displays that the interplanar spacing of the two diffraction rings are about 0.345, 0.269 and 0.19 nm, corresponding to the (211), (310) and (322) lattice plane, respectively. These HRTEM and SAED results confirm formation of crystalline SWO. The low magnification SEM image of SWO/rGO-30 and the corresponding element mapping show uniform distribution of C, O, Sb and W elements, suggesting that SWO is uniformly dispersed in rGO (Fig. S5). In addition, the EDX of SWO/rGO-30 display that the atomic percentage of Sb and W is ~27.9% and ~14%, respectively, which exhibit almost the same Sb/W atomic ratio as $Sb_2WO_6$ (Fig. S6). The O, and C element content from EDX in SEM test are 46.63 at% (10.88 wt%) and 11.43 at% (2.01 wt%), respectively. And the O and C element content from EDX in XPS testing are calculated to be 40.4 at% and 44.5 at%, respectively.

The X-ray photoelectron spectroscopy (XPS) was conducted to investigate the chemical composition and valence-state of SWO/rGO-30 (Fig. 3). SWO/rGO-30 is composed of Sb, W, O, and C elements in Fig. 3a.The C 1s peaks located at 284.8 eV and 286.1 eV could be assigned to C—C and C—OH bonds of rGO, respectively (Fig. 3b) [39]. The binding energy of 530.89 eV and 540.26 eV could be indexed to Sb $3d_{5/2}$ and Sb $3d_{3/2}$ with $3^+$ oxidation state (Fig. 3c) [35,40]. High-resolution W 4f XPS spectra mainly consists of W $4f_{7/2}$ and W $4f_{5/2}$ bands (Fig. 3d), and the two peaks located at 35.64 eV and 38.26 eV correspond to $W^{6+}$ [41]. In addition, in the high-resolution O 1s spectrum, the three peaks centered at 530.88 eV, 532.06 eV and 533.44 eV could be attributed to C=O, O—C and O=C—O, respectively (Fig. S7). [39,42]. The high-resolution Sb 3d XPS spectra of SWO depicted two peaks at 530.26 eV and 539.64 eV, respectively (Fig. S8c) [35,40]. Three fitting peaks of W 4f located at 34.26 eV, 35.64 eV, and 37.64 eV are assigned to $W^{5+}$, $W^{6+}$, $W^{6+}$(Fig. S8d) [43,44]. The $W^{5+}$ in SWO may be attributed to the reduction of $W^{6+}$ by EG, while the GO is reduced to rGO by the EG in SWO/rGO-30 [45]. Compared with XPS peaks in pristine SWO, Sb 3d peaks and W 4f peaks in SWO/rGO-30 show slight shift to the higher energy regions, indicating enhanced conductivity for SWO nanosheets clusters.

Fig. 4a shows cyclic voltammetry curves of SWO/rGO-30 at a scan rate of 0.2 mV $s^{-1}$. Obviously, the irreversible peak centered at ~1.46 V in the first cycle could be attributed to the electrolyte decomposition, conversion reaction of SWO/rGO-30 with $Li^+$, and the formation of solid electrolyte interface (SEI). The peak centered at 0.66 V could be attributed to the alloying reaction of $Li^+$ with Sb [46]. Correspondingly, anodic peaks centered at 1.13 V and 1.4 V could be assigned to the dealloying reaction and the generation of SWO [46]. The overlap of curves in the third and fourth cycles could verify the high reversibility of SWO. Fig. 4b depicts the initial three cycles and the 50th, 100th and 150th galvanostatic charge and discharge cycles of SWO/rGO-30 electrode at 0.2 A $g^{-1}$. The initial specific discharge and charge capacity is ~1141 mAh $g^{-1}$ and ~808 mAh $g^{-1}$, respectively, corresponding to the initial coulombic efficiency of ~70.8%. The low initial coulombic efficiency could be mainly ascribed to SEI formation [47,48]. The almost overlapped curves of the 2nd and 3rd cycles indicate stable reaction mechanism and reversible lithium storage [49]. The voltage plateaus almost remain unchanged and are still corresponding to the CV curves (Fig. 4a) even cycles come to 50, 100, 150 cycles. SWO/rGO-30 electrode could deliver 545.2 mAh $g^{-1}$ at 2 A $g^{-1}$ and 607.7 mAh $g^{-1}$ when the current density turns to 0.2 A $g^{-1}$ (Fig. 4c). Whereas, the SWO electrode could only deliver 322.8 mAh $g^{-1}$ and 383.2 mAh $g^{-1}$ at 2 and 0.2 A $g^{-1}$, respectively. Moreover, SWO/rGO-20 and SWO/rGO-40 exhibit stable discharge capacity of 442.8 mAh $g^{-1}$ and 417.7 mAh $g^{-1}$ at 2 A $g^{-1}$, respectively. Obviously, all SWO/rGO composites show superior capacity than the pristine SWO, indicating that the introduction of rGO in SWO enhances lithium-ion storage. In addition, it is obvious that the SWO/rGO-30 exhibits higher reversible specific capacity than SWO/rGO-20 and SWO/rGO-40, indicating that appropriate addition of rGO could effectively enhance rate capability. The SWO/rGO-20, SWO/rGO-30, and SWO/rGO-40 electrodes could deliver discharge capacity of 464.9 mAh $g^{-1}$, 577.1 mAh $g^{-1}$, and 502.9 mAh $g^{-1}$ after 150 cycles at 0.2 A $g^{-1}$, respectively (Fig. 4d). In contrast, the pristine SWO electrode only delivers 212.5 mAh $g^{-1}$ after 150 cycles. And coulombic efficiencies of SWO and SWO with different GO contents electrodes during cycles at 0.2 A $g^{-1}$ are shown in Fig. 4d, after the first cycle, the coulombic efficiencies gradually grew to >98%, indicating their decent lithium-ion storage reversibility. Moreover, compared with other Sb-based oxides and sulfides, as shown in Table S1, electrochemical performance of SWO/rGO-30 are in comparison with that of recent reported Sb-based oxides and sulfides. Specifically, the capacity of SWO/rGO-30 in this work at 2 A $g^{-1}$ is superior to most Sb-based oxides and sulfides, indicating the excellent conductivity for SWO/rGO hybrid clusters. The SWO/rGO-30 shows favorable cycling performance, but its cycling capacity could be enhanced by robuster host. The improved rate and cycling performance of SWO/rGO-30 can be ascribed to following reasons: Firstly, the introduction of rGO could induce SWO growth

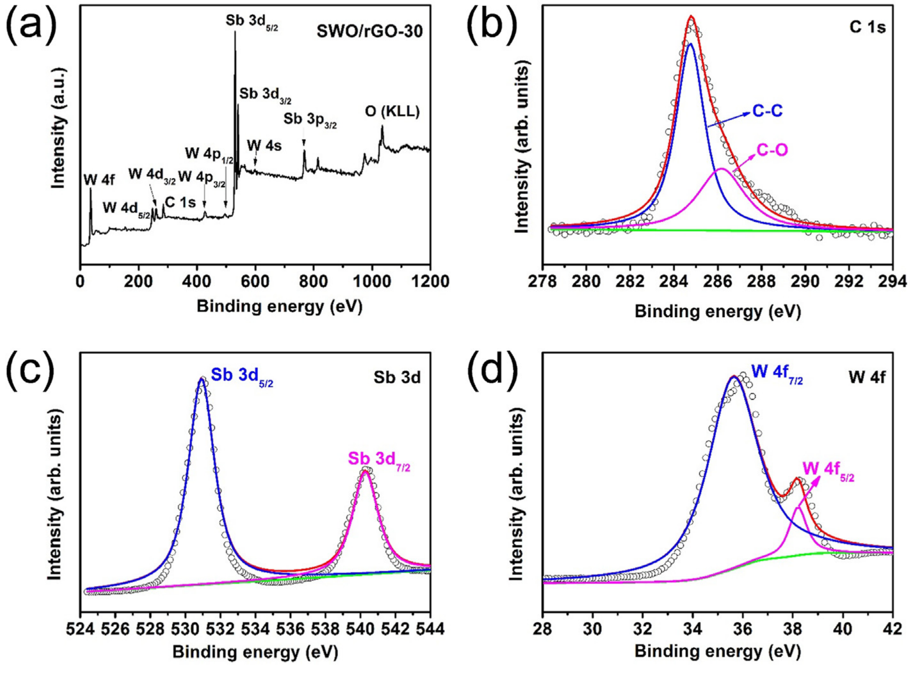

**Fig. 3.** (a) X-ray photoelectron spectroscopy (XPS) survey of SWO/rGO-30, the high-resolution XPS spectra of (b) C 1s, (c) Sb 3d, (d) W 4f.

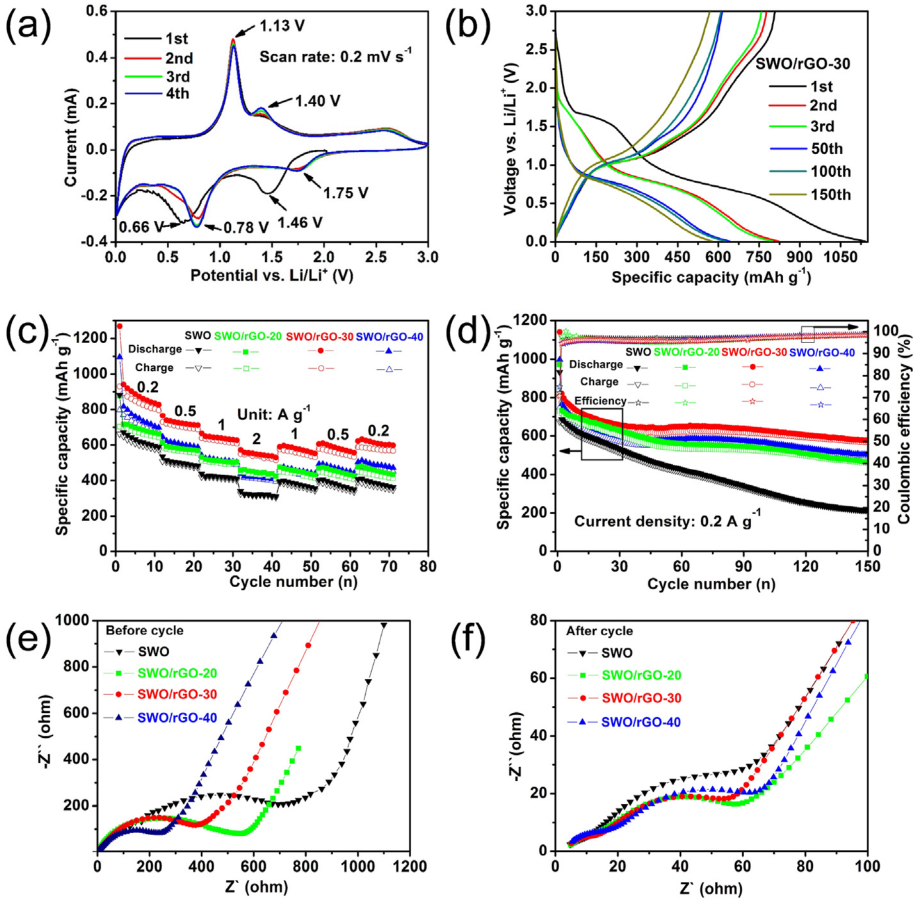

**Fig. 4.** (a) Cyclic voltammetry curves of SWO/rGO-30 electrode at a scan rate of 0.2 mV $s^{-1}$, (b) charge-discharge profiles of SWO/rGO-30 electrode at a current density of 0.2 A $g^{-1}$, (c) rate performance of SWO, and SWO with different GO contents electrodes at current density ranging from 0.2 to 2 A $g^{-1}$, and (d) cycling performances of SWO and SWO with different GO contents electrodes at current density of 0.2 A $g^{-1}$, (e) and (f) the Nyquist spectrum of SWO and SWO with different GO contents electrodes before and after 150 cycles, respectively.

from particles to nanosheets and SWO nanosheets/rGO clusters could provide more lithium storage sites and exhibit faster ion transport [50]. Secondly, rGO in SWO/rGO could improve conductivity and efficiently prevent active materials agglomeration. The qualitative electrochemical kinetics of SWO and SWO with different GO contents electrodes were evaluated by electrochemical impedance spectroscopy (Fig. 4e and f). With increasing rGO content, the charge transfer resistance ($R_{ct}$) of SWO/rGO before cycling gradually decrease due to excellent rGO conductivity (Fig. 4e) [51]. After 150 cycles, the corresponding $R_{ct}$ universally decreased, which could be ascribed to material being activated during cycles. SWO/rGO-30 exhibits the lowest resistance, and the improved electrochemical kinetics of SWO/rGO-30 could mainly result from proper rGO amount whose SWO nanosheets/rGO clusters structure benefits fast lithium-ion transportation.

The surface morphology of SWO and SWO/rGO-30 electrodes before and after 150 cycles at 0.2 A $g^{-1}$ are shown in Figs. S9a–d. SWO and SWO/rGO-30 electrodes before cycling exhibit flat surfaces (Figs. S9a and S9c). After cycles, large cracks are found in SWO electrode (Fig. S9b), which visually indicates the inferior mechanical stability. In sharp contrast, SWO/rGO-30 electrode after 150 cycles exhibits quite compact surface without large cracks (Fig. S9d). The intact surface morphology of SWO/rGO-30 electrode demonstrates excellent mechanical stability and less active material loss.

To further investigate the kinetics process of SWO/rGO-30 electrode, cyclic voltammetry of SWO/rGO-30 electrode were conducted at various scan rates ranging from 0.2 mV $s^{-1}$ to 2 mV $s^{-1}$ (Fig. 5a). The locations of peaks at anodic scanning and cathodic scanning have slightly orientated migration with the scan rate increases. The pseudocapacitive effect could be analyzed through Equations (1) and (2) [52].

$$\mathrm{i(V) = a\,v^b = k_1v + k_2v^{0.5}} \tag{1}$$

$$\log i(V) = b \log v + \log a \tag{2}$$

where i is the current response in CV, V is the voltage value in operating voltage window, $k_1$, $k_2$ and a are constants, and v is the scan rate. Based on the peak current, b values of $\mathrm{Peak_a}$ and $\mathrm{Peak_c}$ at various scan rates were calculated to be 0.73 and 0.87, respectively. These values mean that surface-induced capacitive would be a dominator in SWO/rGO-30 electrode charge storage system (Fig. 5b). Furthermore, the pseudocapacitive contribution proportion can be determined based on Equations (1) and (3) [52,53].

$$i(V) \Big/ v^{0.5} = k_1 v^{0.5} + k_2 \tag{3}$$

Here, the total current response ($i$) at a fixed potential ($V$) can be separated into two mechanisms. The part of $k_1v$ is the surface-

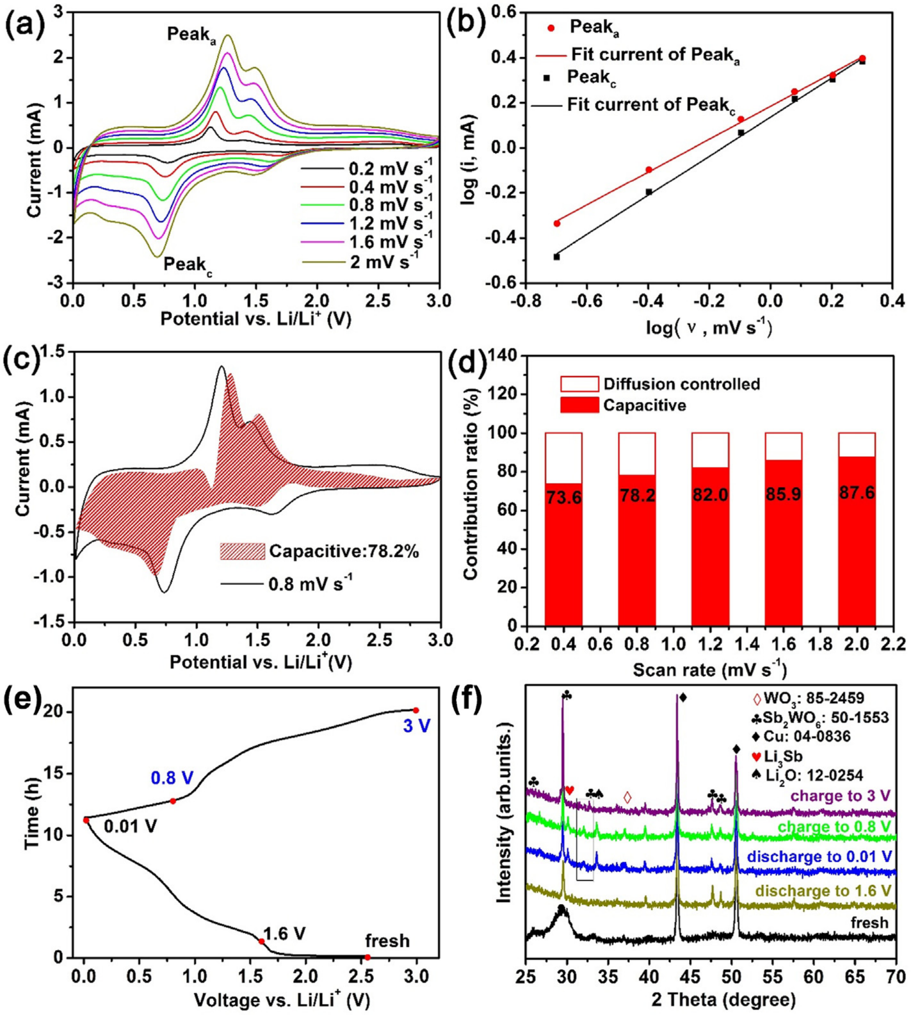

**Fig. 5.** (a) Cyclic voltammetry curves at various scan rates of the SWO/rGO-30 electrode, (b) relationship between sweep rate and peak currents plots for anodic sweeps of CV, (c) diffusion contribution and pseudocapacitive contribution at 0.8 mV s$^{-1}$, (d) diagram of pseudocapacitive contribution and diffusion contribution at various scan rates. (e) discharge-charge profile at 0.1 A g$^{-1}$ in the first cycle, (f) ex-situ XRD patterns of SWO/rGO-30 at different discharge and charge states.

induced capacitive current. The diffusion-controlled current is reflected in $k_2v^{0.5}$ [53]. Fig. 5c indicates that 78.2% of total charge comes from capacitive contribution at a scan rate of 0.8 mV s$^{-1}$ for in SWO/rGO-30. The region is almost pseudocapacitive controlled, which is in accordance with the result of b-value [52]. This obviously implies that mesoporous SWO/rGO-30 nanosheets offer many active surface sites, short lithium ion diffusion pathway as well as good electrolyte accessibility to all the electroactive surfaces, resulting in the excellent electrochemical performance. Moreover, with the scan rate increases, the higher pseudocapacitive contribution percentage, which could ensure excellent rate capacity of SWO/rGO-30 electrode at high current density (Fig. 5d). Fig. S10a displays CV curves of SWO at various scan rates. According to CV curves of SWO (Fig. S10a) and SWO/rGO-30 (Fig. 5a), the Li-ion diffusion coefficient ($D_{Li}$) can be calculated based on the equation: $I_p = 2.69 \times 10^5\ ACD^{1/2}n^{3/2}v^{1/2}$ [54]. Here, $I_p$ is the peak current (A), $A$ represents the anode area (cm$^2$), $C$ stands for the shuttle concentration (mol cm$^{-3}$), $n$ is the number of the involved electrons, $v$ is the scan rate (V s$^{-1}$), and $D_{Li}$ is the diffusion coefficient. Obviously, the $D_{Li}$ is proportional to the ratio of $I_p$ vs $v^{1/2}$. Interestingly, in Fig. S10b, the relationship of $I_p$ vs $v^{1/2}$ is commendably linear, which demonstrates that the electrode reaction is controlled by Li-ion diffusion. As for the slope of $I_p$ vs $v^{1/2}$, it is obvious that the slope of SWO/rGO-30 (0.06603) is higher than the one of the pristine SWO (0.01721). This further demonstrates higher ionic conductivity in SWO/rGO-30 than that in SWO. Based on the above-mentioned formula, the Li-ion diffusion coefficient of SWO/rGO-30 is about $5.3 \times 10^{-9}$ cm$^2$ s$^{-1}$. The favorable diffusion coefficient of SWO/rGO-30 results in excellent electrochemical performance.

To investigate the reaction mechanism of the SWO/rGO-30 electrode during lithium-ion insertion/extraction, the ex-situ XRD was performed during charge/discharge at 0.1 A g$^{-1}$ in 0.01−3V (Fig. 5e and f). As shown in Fig. 5f, when the pristine electrode was discharged to 1.6 V, the crystallization intensity of SWO/rGO-30 enhanced and the $Li_2O$ appeared at 33.56°. The peaks at 43.38° and 50.46° are assigned to the copper current collector. When the SWO/rGO-30 was discharged to 0.01 V, the $Li_3Sb$ and $WO_3$ appeared at 30.08° and 36.97° [55], respectively. This result indicates the conversion reaction and alloy reaction of SWO in LIBs. When the SWO/rGO-30 was charged to 0.8V, the intensity of corresponding XRD peaks of $Li_3Sb$ and $Li_2O$ decreased, indicating the lithium ions extraction. The peaks of $Li_3Sb$, $Li_2O$ and $WO_3$ disappeared completely when the electrode was charged to 3 V. This result demonstrates the reversible lithium-ion insertion/extraction in SWO/rGO-30. Based on above results, the reaction mechanism of SWO in LIBs could be expressed as follows:

$$Sb_2WO_6 + xLi^+ \leftrightarrow Li_xSb_2WO_6 \tag{4}$$

$$Li_xSb_2WO_6 + (12-x)Li^+ \leftrightarrow 2Li_3Sb + WO_3 + 3Li_2O \tag{5}$$

## 4. Conclusion

In summary, SWO nanosheets/rGO clusters have been successfully prepared based on GO inducing SWO growth by the interacted oxygenated groups on GO surface and SWO, and their electrochemical performances as the anode materials in LIBs were systematically investigated. The proper GO content can provide adequate oxygenated groups without GO restacking and transform SWO from particles into nanosheets. In addition, the reliable links between rGO and SWO nanosheets lead to enhanced electronic conductivity and ionic conductivity. The SWO nanosheets/rGO clusters can effectively prevent the aggregation of SWO nanosheets to provide stable active sites and relieve volume changes during cycling. The SWO/rGO-30 clusters exhibit superior rate and cycle performance. When the current density is 2 A $g^{-1}$, the SWO/rGO-30 clusters could still deliver the discharge specific capacity of 545.2 mAh $g^{-1}$. Overall, the SWO/rGO-30 clusters could be used as a promising negative electrode material for high-energy-density LIBs.

## Declaration of competing interest

The authors declare that they have no known competing financial interests or personal relationships that could have appeared to influence the work reported in this paper.

## CRediT authorship contribution statement

**Fei Wang:** Methodology, Investigation, Writing - original draft. **Yong Liu:** Conceptualization, Writing - review & editing, Supervision. **Huijie Wei:** Investigation, Writing - original draft. **Guangxin Wang:** Funding acquisition. **Fengzhang Ren:** Conceptualization, Supervision, Funding acquisition. **Xianming Liu:** Methodology. **Min Chen:** Investigation. **Alex A. Volinsky:** Writing - review & editing. **Shizhong Wei:** Funding acquisition. **Yan-Bing He:** Conceptualization, Writing - review & editing, Supervision.

## Acknowledgements

This work was supported by Program for Changjiang Scholars and Innovative Research Team in University (IRT_16R21), the Chinese 02 Special Fund (2017ZX02408003), the Scientific and Technological Project of Henan Province (182102210297), Open Fund of National Joint Engineering Research Center for abrasion control and molding of metal materials (HKDNM201807), the Student Research Training Plan of Henan University of Science and Technology (2019031), and Shenzhen Technical Plan Project (Nos. JCYJ20170412170706047 and JCYJ20180508152135822). This work was also supported by Shenzhen Graphene Manufacturing Innovation Center (No. 201901161513).

## Appendix A. Supplementary data

Supplementary data to this article can be found online at https://doi.org/10.1016/j.jallcom.2020.155614.

## References

[1] S. Chu, Y. Cui, N. Liu, The path towards sustainable energy, Nat. Mater. 16 (2017) 16–22.

[2] D. Larcher, J.M. Tarascon, Towards greener and more sustainable batteries for electrical energy storage, Nat. Chem. 7 (2015) 19–29.

[3] Y.X. Tang, Y.Y. Zhang, W.L. Li, B. Ma, X.D. Chen, Rational material design for ultrafast rechargeable lithium-ion batteries, Chem. Soc. Rev. 44 (2015) 5926–5940.

[4] A.S. Arico, P. Bruce, B. Scrosati, J.-M. Tarascon, W. van Schalkwijk, Nanostructured materials for advanced energy conversion and storage devices, Nat. Mater. 4 (2005) 366–377.

[5] J.C. Zheng, Z. Yang, Z.J. He, H. Tong, W.J. Yu, J.F. Zhang, In situ formed $LiNi_{0.8}Co_{0.15}Al_{0.05}O_2@Li_4SiO_4$ composite cathode material with high rate capability and long cycling stability for lithium-ion batteries, Nano Energy 53 (2018) 613–621.

[6] F. Wang, Y. Liu, Y.F. Zhao, Y. Wang, Z.J. Wang, W.H. Zhang, et al., Facile synthesis of two-dimensional porous $MgCo_2O_4$ nanosheets as anode for lithium-ion batteries, Appl. Sci. Basel 8 (2018) 8010022.

[7] Y. Liu, H.C. Wang, K.K. Yang, Y.N. Yang, J.Q. Ma, K.M. Pan, et al., Enhanced electrochemical performance of $Sb_2O_3$ as an anode for lithium-ion batteries by a stable cross-linked binder, Appl. Sci. Basel 9 (2019) 9132677.

[8] Z. Li, Q.F. Yin, W.W. Hu, J.W. Zhang, J.H. Guo, J.P. Chen, et al., Tin/tin antimonide alloy nanoparticles embedded in electrospun porous carbon fibers as anode materials for lithium-ion batteries, J. Mater. Sci. 54 (2019) 9025–9033.

[9] Y.Y. Wang, Z.J. Wang, D.N. Lei, W. Lv, Q. Zhao, B. Ni, et al., Spherical Li deposited inside 3D Cu skeleton as anode with ultrastable performance, ACS Appl. Mater. Interfaces 10 (2018) 20244–20249.

[10] X.D. Ma, X.H. Xiong, P.J. Zou, W.Z. Liu, F. Wang, L.W. Liang, et al., General and scalable fabrication of core-shell metal sulfides@C anchored on 3D N-doped foam toward flexible sodium ion batteries, Small 15 (2019) 1903259.

[11] C.B. Zhu, X.K. Mu, P.A. van Aken, J. Maier, Y. Yu, Fast Li storage in $MoS_2$-graphene-carbon nanotube nanocomposites: advantageous functional integration of 0D, 1D, and 2D nanostructures, Adv. Energy Mater. 5 (2015) 1401170.

[12] J. Liu, Y.R. Wen, Y. Wang, P.A. van Aken, J. Maier, Y. Yu, Carbon-encapsulated pyrite as stable and earth-abundant high energy cathode material for rechargeable lithium batteries, Adv. Mater. 26 (2014) 1401496.

[13] G.L. Liu, J. Cui, R.J. Luo, Y. Liu, X.X. Huang, N.T. Wu, et al., 2D $MoS_2$ grown on biomass-based hollow carbon fibers for energy storage, Appl. Surf. Sci. 469 (2019) 854–863.

[14] H.K. Wang, X.M. Yang, Q.Z. Wu, Q.B. Zhang, H.X. Chen, H.M. Jing, et al., Encapsulating silica/antimony into porous electrospun carbon nanofibers with robust structure stability for high-efficiency lithium storage, ACS Nano 12 (2018) 3406–3416.

[15] P.J. Zou, Z.H. Lin, M.N. Fan, F. Wang, Y. Liu, X.H. Xiong, Facile and efficient fabrication of Li3PO4-coated Ni-rich cathode for high-performance lithium-ion battery, Appl. Surf. Sci. 504 (2020), 144506.

[16] C. Zeng, W. Weng, T. Lv, W. Xiao, Low-temperature assembly of ultrathin amorphous $MnO_2$ nanosheets over $Fe_2O_3$ spindles for enhanced lithium storage, ACS Appl. Mater. Interfaces 10 (2018) 30470–30478.

[17] S. Zhu, J.J. Li, X.Y. Deng, C.N. He, E.Z. Liu, F. He, et al., Ultrathin-nanosheet-induced synthesis of 3D transition metal oxides networks for lithium ion battery anodes, Adv. Funct. Mater. 27 (2017).

[18] X.F. Chen, Y. Huang, K.C. Zhang, X.S. Feng, M.Y. Wang, Porous $TiO_2$ nanobelts coated with mixed transition-metal oxides $Sn_3O_4$ nanosheets core-shell composites as high-performance anode materials of lithium ion batteries, Electrochim. Acta 259 (2018) 131–142.

[19] P. Poizot, S. Laruelle, S. Grugeon, L. Dupont, J.M. Tarascon, Nano-sized transition-metal oxides as negative-electrode materials for lithium-ion batteries, Nature 407 (2000) 496–499.

[20] C.Z. Yuan, H.B. Wu, Y. Xie, X.W. Lou, Mixed transition-metal oxides: design, synthesis, and energy-related applications, Angew. Chem. Int. Ed. 53 (2014) 1488–1504.

[21] J. Lee, C. Jo, B. Park, W. Hwang, H.I. Lee, S. Yoon, Simple fabrication of flexible electrodes with high metal-oxide content: electrospun reduced tungsten oxide/carbon nanofibers for lithium ion battery applications, Nanoscale 6 (2014) 10147–10155.

[22] Y.Y. Sun, Y.H. Zou, F. Yuan, C.Y. Yan, S. Chen, Y.A. Jia, et al., Controllable synthesis of a peapod-like nanostructure via nanoconfining CoFe2O4 in CMK-5 for high-performance lithium-ion batteries, Appl. Surf. Sci. 467 (2019) 640–647.

[23] Z.M. Zheng, P. Li, J.S. Huang, H.D. Liu, Y. Zao, Z.L. Hu, et al., High performance columnar-like $Fe_2O_3$@carbon composite anode via yolk@shell structural design, J. Energy Chem. 41 (2020) 126–134.

[24] A. Singh, D.P. Dutta, M. Roy, A.K. Tyagi, M.H. Fulekar, Sonochemical synthesis, characterization, and photocatalytic properties of $Bi_{2-x}Sb_{(x)}WO_6$ nanorods, J. Mater. Sci. 49 (2014) 2085–2097.

[25] C.Y. Yang, X.J. Yang, F. Li, T.H. Li, W. Cao, Controlled synthesis of hierarchical flower-like $Sb_2WO_6$ microspheres: photocatalytic and superhydrophobic property, J. Ind. Eng. Chem. 39 (2016) 93–100.

[26] S.P. Hu, C.Y. Xu, F.X. Ma, L. Cao, L. Zhen, Solvothermal synthesis of orthorhombic $Sb_2WO_6$ hierarchical structures and their visible-light-driven photocatalytic activity, Dalton Trans. 43 (2014) 8439–8445.

[27] M.D.L. Cruz, F.E.L. Rodríguez, Electrochemical lithium insertion in the solid

solution $Bi_2WO_6$ -$Sb_2WO_6$ with Aurivillius framework, Mater. Res. Bull. 42 (2007) 1851–1855.

[28] Y. Liu, Y. Wang, F. Wang, Z. Lei, W. Zhang, K. Pan, J. Liu, M. Chen, G. Wang, F. Ren, S. Wei, Facile synthesis of antimony tungstate nanosheets as anodes for lithium-ion batteries, Nanomaterials 9 (2019) 1689.

[29] P. Wang, S.M. Xie, Y.Y. She, W.G. Fan, M.K.H. Leung, H.K. Wane, Microwave-hydrothermal synthesis of hierarchical $Sb_2WO_6$ nanostructures as a new anode material for sodium storage, Chemistryselect 4 (2019) 1078–1083.

[30] J.J. Wang, L.Y. Wang, S.Y. Zhang, S.Y. Liang, X.Q. Liang, H.F. Huang, et al., Facile synthesis of iron-doped $SnO_2$/reduced graphene oxide composite as high-performance anode material for lithium-ion batteries, J. Alloys Compd. 748 (2018) 1013–1021.

[31] A.A. AbdelHamid, Y. Yu, J.H. Yang, J.Y. Ying, Generalized synthesis of metal oxide nanosheets and their application as Li-ion battery anodes, Adv. Mater. 29 (2017) 1701427.

[32] C.L. Zhang, Y. Xu, M. Zhou, L.Y. Liang, H.S. Dong, M.H. Wu, Y. Yang, Y. Lei, Potassium prussian blue nanoparticles: a low-cost cathode material for potassium-ion batteries, Adv. Funct. Mater. 27 (2017) 1604307.

[33] S. Yuvaraj, G.K. Veerasubramani, M.S. Park, P. Thangave, D.W. Kim, Facile synthesis of FeS2/MoS2 composite intertwined on rGO nanosheets as a high-performance anode material for sodium-ion battery, J. Alloys Compd. 821 (2020) 153222.

[34] Q.H. Wang, C. Guo, Y.X. Zhu, J.P. He, H.Q. Wang, Reduced graphene oxide-wrapped FeS2 composite as anode for high-performance sodium-ion batteries, Nano-Micro Lett. 10 (2018) 30.

[35] Q. Liu, Y.W. Yan, X.C. Chu, Y.L. Zhang, L.H. Xue, W.X. Zhang, Graphene-induced growth of single crystalline $Sb_2MoO_6$ sheets and their sodium storage performance, J. Mater. Chem. 5 (2017) 21328–21333.

[36] H.C. Park, K.H. Lee, Y.W. Lee, S.J. Kim, D.M. Kim, M.C. Kim, et al., Mesoporous molybdenum nitride nanobelts as an anode with improved electrochemical properties in lithium ion batteries, J. Power Sources 269 (2014) 534–541.

[37] J.R. Rani, R. Thangavel, S.-I. Oh, Y.S. Lee, J.-H. Jang, An ultra-high-energy density supercapacitor; fabrication based on thiol-functionalized graphene oxide scrolls, Nanomaterials 9 (2019) 148.

[38] L. Li, R.Y. Chen, Y.J. Gong, C.Y. Yu, Z.Y. Hui, H. Xu, et al., Assembling laminated films via the synchronous reduction of graphene oxide and formation of copper-based metal organic frameworks, J. Mater. Chem. 7 (2019) 107–111.

[39] A.M. Jastrzebska, J. Karcz, R. Letmanowski, D. Zabost, E. Ciecierska, J. Zdunek, et al., Synthesis of the RGO/$Al_2O_3$ core-shell nanocomposite flakes and characterization of their unique electrostatic properties using zeta potential measurements, Appl. Surf. Sci. 362 (2016) 577–594.

[40] X. Lu, Z.Y. Wang, L. Lu, G. Yang, C.M. Niu, H.K. Wang, Synthesis of hierarchical $Sb_2MoO_6$ architectures and their electrochemical behaviors as anode materials for Li-ion batteries, Inorg. Chem. 55 (2016) 7012–7019.

[41] X. Wu, S.Y. Yao, Flexible electrode materials based on $WO_3$ nanotube bundles for high performance energy storage devices, Nano Energy 42 (2017) 143–150.

[42] H.L. Shen, X.F. Xia, Y. Ouyang, X.Y. Jiao, S. Mutahir, D.N. Mandler, et al., Preparation of biomass-based porous carbons with high specific capacitance for applications in supercapacitors, Chemelectrochem 6 (14) (2019) 3599–3605.

[43] W.J. Duan, J.B. Wang, X.L. Zhong, High nonlinearity in $WO_x$ film prepared by hydrazine hydrate reduction method, Mater. Lett. 211 (2018) 62–64.

[44] L. Yang, H.X. Liao, Y. Tian, W.W. Hong, P. Cai, C. Liu, et al., Rod-Like $Sb_2MoO_6$: structure evolution and sodium storage for sodium-ion batteries, Small Methods 3 (2018) 1800533.

[45] Y.M. Huang, J.X. Ouyang, X. Tang, Y. Yang, J.F. Qian, J.T. Lu, et al., $NiGa_2O_4$/rGO composite as long-cycle-life anode material for lithium-ion batteries, ACS Appl. Mater. Interfaces 11 (2019) 8025–8031.

[46] J.J. Xie, L. Liu, J. Xia, Y. Zhang, M. Li, Y. Ouyang, et al., Template-free synthesis of $Sb_2S_3$ hollow microspheres as anode materials for lithium-ion and sodium-ion batteries, Nano-Micro Lett. 10 (2018) 1701651.

[47] A.P. Wang, S. Kadam, H. Li, S.Q. Shi, Y. Qi, Review on modeling of the anode solid electrolyte interphase (SEI) for lithium-ion batteries, NPJ Comput. Mater. 4 (2018) 1800640.

[48] J.B. Goodenough, Y. Kim, Challenges for rechargeable Li batteries, Chem. Mater. 22 (2010) 587–603.

[49] Z.M. Zheng, Y. Zao, Q.B. Zhang, Y. Cheng, H.X. Chen, K.L. Zhang, et al., Robust erythrocyte-like $Fe_2O_3$@carbon with yolk-shell structures as high-performance anode for lithium ion batteries, Chem. Eng. J. 347 (2018) 563–573.

[50] G. Wang, J. Zhang, S. Yang, F.X. Wang, X.D. Zhuang, K. Mullen, et al., Vertically aligned $MoS_2$ nanosheets patterned on electrochemically exfoliated graphene for high-performance lithium and sodium storage, Adv. Energy Mater. 8 (2018) 1702254.

[51] J.B. Chang, X.K. Huang, G.H. Zhou, S.M. Cui, P.B. Hallac, J.W. Jiang, et al., Multilayered Si nanoparticle/reduced graphene oxide hybrid as a high-performance lithium-ion battery anode, Adv. Mater. 26 (2014) 758–764.

[52] J. Wang, J. Polleux, J. Lim, B. Dunn, Pseudocapacitive contributions to electrochemical energy storage in $TiO_2$ (anatase) nanoparticles, J. Phys. Chem. C 111 (2007) 14925–14931.

[53] R.M. Sun, S.J. Liu, Q.L. Wei, J.Z. Sheng, S.H. Zhu, Q.Y. An, L.Q. Mai, Mesoporous NiS2 nanospheres anode with pseudocapacitance for high-rate and long-life sodium-ion battery, Small 13 (2019) 1701744.

[54] J. Liu, L.T. Yu, C. Wu, Y.R. Wen, K.B. Yin, F.K. Chiang, et al., New nanoconfined galvanic replacement synthesis of hollow Sb@C yolk-shell spheres constituting a stable Anode for high-rate Li/Na-ion batteries, Nano Lett. 17 (2017) 2034–2042.

[55] X.M. Zhao, W.Q. Rong, J.H. You, G.P. Tu, P.Y. Zhang, S. Tao, et al., An electrodeposition strategy for the controllable and cost-effective fabrication of Sb-Fe-P anodes for Li ion batteries, Electrochim. Acta 309 (2019) 469–476.